

UKAEA-CCFE-PR(19)73

David Schworer, Nick Walkden, Ben Dudson, Fulvio
Militello, Huw Leggate, Miles Turner

Dynamics of Scrape-off Layer Filaments in Detached Conditions

Enquiries about copyright and reproduction should in the first instance be addressed to the UKAEA Publications Officer, Culham Science Centre, Building K1/O/83 Abingdon, Oxfordshire, OX14 3DB, UK. The United Kingdom Atomic Energy Authority is the copyright holder.

The contents of this document and all other UKAEA Preprints, Reports and Conference Papers are available to view online free at <https://scientific-publications.ukaea.uk/>

Dynamics of Scrape-off Layer Filaments in Detached Conditions

David Schworer, Nick Walkden, Ben Dudson, Fulvio Militello,
Huw Leggate, Miles Turner

Dynamics of scrape-off layer filaments in detached conditions

D. Schwörer^{a,b}, N. R. Walkden^b, B. D. Dudson^c,
F. Militello^b, H. Leggate^a, M. M. Turner^a

^aDublin City University, Dublin 9, Ireland

^bCCFE, Culham Science Centre, Abingdon, Oxfordshire, OX14 3DB, UK

^cYork Plasma Institute, Department of Physics, University of York, Heslington, York YO10 5DQ, UK

E-mail: david.schworer2@mail.dcu.ie

3 September 2019

Abstract. The here presented work studies the dynamics of filaments using 3D full-f fluid simulations in the presence of detached background profiles. It was found that evolving the neutrals on the time-scale of the filament did not have a significant impact on the dynamics of the filament. In general a decreasing filament velocity with increasing plasma density has been observed, with the exception of detachment onset, where a temporarily increase in radial velocity occurs. This was found for filaments around the critical size and larger, while smaller filaments were less affected by detachment. With detachment the critical filament size increased, as larger filaments were faster in detached conditions. This breaks the trend of attached conditions, where the critical size decreases with increasing density.

1. Introduction

Filaments are field aligned pressure perturbations, observed in the tokamaks scrape-off layer (SOL), that have a much higher amplitude than the background fluctuations. They have been observed in most magnetized plasmas, including most fusion devices, where various properties of SOL fluctuations have been measured, for example the skewed probability distribution function [1, 2]. In the SOL of tokamaks, filaments have been observed to cause a significant amount of transport across the magnetic field [3]. Filaments can be modelled non-linearly in two dimensions, evolving two fields, namely the density and the vorticity [1, 4, 5]. In this case the lack of the third dimension, parallel to the magnetic field, is typically closed by the advection closure or the sheath closure [5]. This has been extended in various ways in recent years, e.g. including the full parallel dynamics, which is required for capturing drift waves, and capturing sheath dynamics [5–7].

The dynamics of filaments has a dependence on their perpendicular size δ_{\perp} . While for small filaments a significant amount of the diamagnetic current across the filament is closed via currents in the drift-plane, sheath currents are important for large filaments [1, 5]. The radial velocity has a maximum at a specific size - referred to as the critical size δ^* , which represents a balance point between these two closure paths.

A major challenge for the operation of fusion devices, such as ITER, is the power handling in the divertor. ITER will thus have to operate in detached, or at least partially detached conditions [8]. Detachment is an operational regime in which the heat and particle target fluxes are reduced, as a significant part of the plasma is cooled before it can reach the target [9, 10]. Detached conditions require a drop of total plasma pressure along the flux tube. Charge-exchange can be an efficient sink for plasma momentum as well as a sink for the plasma energy, reducing the heat load at the target, as well as reducing the density flux. A common condition to define detachment is the so called roll-over [8, 11]. As the upstream density is increased, during attached operation the particle target flux increases. As detachment is reached, the particle target flux drops with increasing upstream density, as a result of the loss of pressure in the vicinity of the target.

As detachment is reached the plasma temperature drops significantly in the vicinity of the target. This causes an increased plasma resistivity. Easy *et al* found by introducing an artificially increased resistivity an increased radial filament velocity. As well as increased radial velocity, an increased critical size δ^* was observed with increasing viscosity [12].

Filaments are a significant cross field transport mechanism and have been shown that they significantly influence the time averaged profiles [13, 14]. At the same time filaments depend on the background condition. In order to understand this non-trivial interaction, an increased understanding of filament dynamics in detached conditions is required.

Our previous study found the importance of realistic background profiles for the dynamics of filaments, where a strong dependence of the target temperature has been observed in attached conditions [15]. In the attached conditions, only a weak influence of neutrals on the dynamic of filaments has been observed. The increased resistivity by a decreased temperature did not result in an increased velocity, as the change in target temperature had a stronger effect [5, 15]

This work aims to extend this into detached conditions, as it is expected that the filament-neutrals interaction will become important in the higher density cases. This also allows to extend the resistivity of the background plasma in a self-consistent way to levels studied by Easy *et al*.

The model used will be introduced in sec. 2. After a short introduction to the backgrounds profiles in sec. 3, the results of the simulations are presented in sec. 4. The simulation include the direct influence of neutrals (sec. 4.1), the impact of detachment on the radial velocity (sec. 4.2) and on the critical size (sec. 4.3) as well as the rigidity of filaments (sec. 4.4). The results will be discussed in sec. 5, before a short summary is given ins sec. 6.

2. Model

STORM is a 2 fluid, full-f plasma model for the study of filaments [5, 12, 16, 17] implemented using the MPI parallelised library BOUT++ [18, 19]. BOUT++ allows a user to implement fluid models in curvi-linear geometry in close to analytical form. BOUT++ is open source, published under the LGPL license, and thus freely available ‡. STORM has recently been extended to include neutrals [15, 17]. The neutrals models have been implemented using an object oriented approach, providing

‡ <https://boutproject.github.io/>

a common interface, from which the actual implementations are derived. This allows the user to easily switch on and off the neutrals, or change the neutrals model, even at run time. It further allows to separate the neutral model development from the development of STORM. Finally, this allows to use the neutrals model in other projects, as the neutrals model has a simple interface, allowing fast integration.

The neutral model consists of the density of the neutrals atoms n_n , of which the logarithm is evolved.

$$\frac{\partial \log(n_n)}{\partial t} = \frac{1}{n_n} (-\nabla_{\parallel} m_n + S_R + \Gamma^{\text{rec}} - \Gamma^{\text{ion}} + -\nabla_{\parallel} \mu_{n_n} \cdot \nabla_{\parallel} n_n) - f_l \quad (1)$$

and the velocity v_n along the magnetic field lines, for which the momentum m_n is evolved

$$\begin{aligned} \frac{\partial m_n}{\partial t} = & \nabla_{\parallel} v_n m_n + \nabla_{\parallel} n_n T_n + \Gamma^{\text{rec}} U \\ & + \Gamma^{\text{CX}}(U - v_n) - \Gamma^{\text{ion}} v_n + \mu_{m_n} \nabla_{\parallel}^2 m_n + S_R v_{th} \end{aligned} \quad (2)$$

The charge exchange, ionisation and recombination rates are denoted by Γ^{CX} , Γ^{ion} and Γ^{rec} respectively. The model is similar to the UEDGE fluid model [20]. As the plasma flows are strongly field aligned, evolving the parallel velocity of the neutrals allows to model the friction in a momentum conserving way. As the background are only one dimensional, the inclusion of perpendicular velocities of the neutrals would thus have no impact on the backgrounds. S_R is the source due to recycling, which is a Gaussian function located at the target. The integral over which sums to 99% of the particle target flux. μ_{n_n} is the neutral diffusion, and f_l is a loss fraction, compensating the lack of cross-field losses. The temperature of the neutrals T_n is not evolved, and is assumed to be 3 eV, close to the Franck-Condon energy [21], with the associated thermal speed v_{th} . Evolving the logarithm of the density, rather than the density itself is beneficial for the stability of the code. As the neutral density can vary quite strongly within a small spatial region, this is of importance for running simulation in detached conditions. The logarithm further ensures that the density-solution always remains positive. Using the logarithm also changes the error norm, which matters as an iterative solver is used to evolve the system. This ensures that the solution is accurate, even in the presence of low densities. For the recycling, in previous models an exponential function was chosen. As a strong decay is preferred to model the recycling in detached conditions, this caused a strong finite-size dependence, as the gradient is highest next to the target, thus refining the grid causes the neutrals to be deposited increasingly close to the target. This is avoided by switching to a Gaussian function. It still retains the strong drop-off further away from the target. Further, the strong gradients near the sheath boundary conditions, due to detachment, need to be resolved. Thus the mesh contained 480 points in parallel direction, giving a uniform grid spacing of ≈ 2.1 cm, significantly refined compared to previous studies [5, 15].

The geometry used is a simple slab geometry, with x being the radial coordinate, z being the parallel direction, and y being the bi-normal direction. Only half of the flux tube is simulated, thus symmetry boundary conditions are used at the mid-plane [15]. At the target sheath boundary conditions are applied, requiring the ion velocity to reach the speed of sound c_s , and the electrons $c_s \exp(-V_f - \frac{\phi}{T})$. The STORM equation

describing the plasma consist of the density n equation for the electrons

$$\frac{\partial n}{\partial t} = \frac{\nabla\phi \times \vec{b}}{B} \cdot \nabla n - \nabla_{\parallel}(Vn) + \mu_n \nabla^2 n - gn \frac{\partial\phi}{\partial y} + g \frac{\partial n T}{\partial y} + \Gamma^{\text{ion}} - \Gamma^{\text{rec}} \quad (3)$$

where ϕ denotes the potential, which is the Laplacian inversion $\omega = \nabla_{\perp}^2 \phi$ of the vorticity. The magnetic field of direction \vec{b} and magnitude $B = 0.5 \text{ T}$. μ_{α} is the diffusion rate for quantity α , so μ_n denotes the diffusion rate for the density. g is the effective gravity constant playing the role of magnetic curvature. g is related to the major radius R_c which is set to 1.5 m thus $g = \frac{2}{R_c} \approx 1.33 \text{ m}^{-1}$. Both R_c and B were chosen to be representative of MAST. The terms containing g are drive terms. The equation for the parallel electron velocity V is

$$\begin{aligned} \frac{\partial V}{\partial t} = & \frac{\nabla\phi \times \vec{b}}{B} \cdot \nabla V - V \nabla_{\parallel} V + \mu \nabla_{\parallel} \phi - \frac{\mu}{n} \nabla_{\parallel} n T \\ & + n \mu \eta_{\parallel} (U - V) - 0.71 \mu \nabla_{\parallel} T - \frac{V}{n} \Gamma^{\text{ion}} + \mu_{\parallel} \nabla_{\parallel}^2 V \end{aligned} \quad (4)$$

with the ion-electron mass ratio is $\mu = m_i/m_e$. The parallel ion-electron resistivity is given by η_{\parallel} . Electron neutral collisions are neglected, as they only become important below 1 eV [12]. The viscosity term μ_{\parallel} was introduced to improve the numerical stability, with the magnitude well below the Braginskii level [22]. The equation for the parallel ion velocity U

$$\begin{aligned} \frac{\partial U}{\partial t} = & \frac{\nabla\phi \times \vec{b}}{B} \cdot \nabla U - U \nabla_{\parallel} U - \nabla_{\parallel} \phi - \eta_{\parallel} n (U - V) \\ & + 0.71 \nabla_{\parallel} T - \frac{U}{n} \Gamma^{\text{ion}} - \frac{U}{n} \Gamma^{\text{CX}} + \mu_{\parallel} \nabla_{\parallel}^2 U \end{aligned} \quad (5)$$

the equation for the electron temperature T

$$\begin{aligned} \frac{\partial T}{\partial t} = & \frac{\nabla\phi \times \vec{b}}{B} \cdot \nabla T - V \nabla_{\parallel} T + \frac{2}{3} \left(\frac{-1}{n} \nabla_{\parallel} q_{\parallel} + 0.71 (U - V) \nabla_{\parallel} T - T \nabla_{\parallel} V \right. \\ & \left. + \frac{\kappa_{\perp}}{n} \nabla_{\perp}^2 T + \eta_{\parallel} n (U - V)^2 + \mu_{\parallel} \frac{V}{n} \nabla_{\parallel}^2 V \right) - \frac{2}{3} g T \frac{\partial\phi}{\partial y} - \frac{2}{3} g \frac{T^2}{n} \frac{\partial n}{\partial y} - \frac{7}{3} g T \frac{\partial T}{\partial y} \\ & - \frac{2}{3} g V^2 \frac{1}{\mu n} \frac{\partial n T}{\partial y} - \frac{T}{n} \Gamma^{\text{ion}} - \frac{T}{n} \Gamma^{\text{CX}} - \frac{1.09 T - 13.6 eV}{n} \Gamma^{\text{rec}} - \frac{30 eV}{n} \Gamma^{\text{ion}} - R^{\text{imp}} \end{aligned} \quad (6)$$

The parallel heat conduction is given by q_{\parallel} and κ_{\perp} is the perpendicular heat transport coefficient. The impurity radiation R^{imp} is using the carbon radiation model from Hutchinson [9] using an impurity fraction of 1%. The radiation seems to have only a minor impact, and is not responsible for the total plasma pressure drop in front of the target. The equation for the vorticity ω is

$$\begin{aligned} \frac{\partial \omega}{\partial t} = & \frac{\nabla\phi \times \vec{b}}{B} \cdot \nabla \omega - U \nabla_{\parallel} \omega + \nabla_{\parallel} (U - V) + \frac{U - V}{n} \nabla_{\parallel} n + \mu_{\omega} \nabla^2 \omega \\ & + \nabla_{\perp} \mu_{\omega} \cdot \nabla_{\perp} \omega + \frac{g}{n} \frac{\partial n T}{\partial y} - \frac{1}{n} \nabla_{\perp}^2 \phi (\Gamma^{\text{CX}} + \Gamma^{\text{ion}}) - \frac{1}{n} \nabla_{\perp} \phi \cdot \nabla_{\perp} (\Gamma^{\text{CX}} + \Gamma^{\text{ion}}) \end{aligned} \quad (7)$$

The cross field transport coefficients are calculated self consistently, following the derivation of Fundamenski *et al* [15, 23]. Further details about the model are given in reference [15]. The neutral terms in the vorticity equation (7) provide a closure for the drive. In order to derive a scaling for this closure, we follow the approach of Walkden *et al* [16] and balance the drive term with the neutrals closure:

$$\frac{g}{n} \frac{\partial n T}{\partial y} \sim \frac{1}{n} \nabla_{\perp}^2 \phi (\Gamma^{\text{CX}} + \Gamma^{\text{ion}}) + \frac{1}{n} \nabla_{\perp} \phi \cdot \nabla_{\perp} (\Gamma^{\text{CX}} + \Gamma^{\text{ion}}) \quad (8)$$

Replacing derivatives by the inverse filament size

$$g \frac{\delta p}{\delta_{\perp}} \sim \frac{\phi (\Gamma^{\text{CX}} + \Gamma^{\text{ion}})}{\delta_{\perp}^2} \quad (9)$$

$$\phi \sim \delta p \frac{g \delta_{\perp}}{\Gamma^{\text{CX}} + \Gamma^{\text{ion}}} \quad (10)$$

we get the filament velocity

$$v_r \sim \delta p \frac{g}{\Gamma^{\text{CX}} + \Gamma^{\text{ion}}} \quad (11)$$

Thus if the vorticity is closed mainly by the neutrals, the filament velocity should have no size dependence. For filaments in the viscous regime, scaling of δ_{\perp}^2 is expected. In the inertial regime, a scaling of $\delta_{\perp}^{\frac{3}{2}}$ is expected, and in the sheath limited regime, a scaling of δ_{\perp}^{-2} is expected, thus the neutral scaling lies between the inertial and sheath limited regime, and is expected to be the dominant closing mechanism for large filaments, that are not able to connect to the sheath.

As will be shown later, the filament velocity does not reach a constant velocity for large filament, but rather a decrease of radial velocity with increasing size is observed. The above derivation did not include the spatial distribution of neutrals, and thus of the neutral interaction rates of the vorticity $\Gamma = \Gamma^{\text{CX}} + \Gamma^{\text{ion}}$. We assume for simplicity a single current path, that flows from the filament, along the field lines, into the detached region, via the neutrals in a single drift plane, and up along the field lines.

In the parallel part, the voltage drops by ϕ_{\parallel} to get through the resistivity $\int_0^z \Gamma n \eta dz$. For the neutrals the voltage drops by ϕ_{\perp} and results in the vorticity sink $\Gamma \phi_{\perp} \delta_{\perp}^{-2}$

The neutral-plasma interaction was modified, to study the filament-neutrals interaction in more detail. In the “full neutral” model, the neutrals are evolved, using the equations above, and the interaction rates Γ^{α} are calculated self consistently. In the “static neutral” model, the neutrals are kept at their steady state values, and the interaction rate Γ^{α} are calculated based on plasma and neutral distribution. In the “no interaction” model, the neutral contribution to the vorticity equation is dropped.

3. Background profiles

In order to run the filament simulations, 1D backgrounds along the parallel direction were computed using the equations described in section 2. An upstream density and energy source is included which are exponentially shaped and located at the mid-plane. The density source was controlled with a PID controller to achieve a predefined density

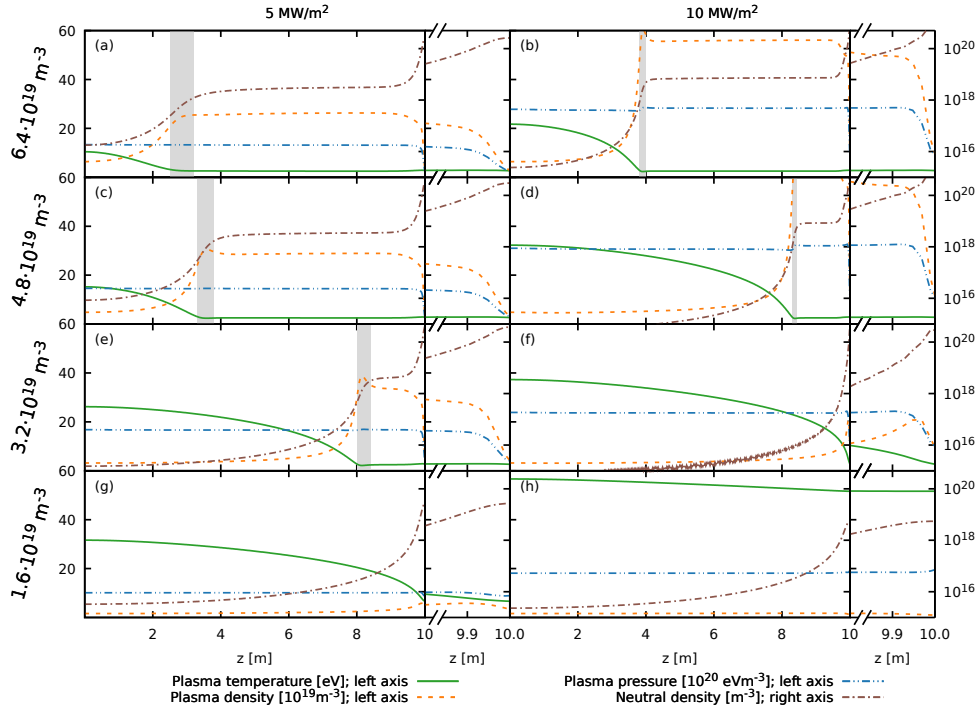


Figure 1: Background plasma profiles, run to steady-state for a set energy influx P_i and density n_0 . The sheath is at the right hand side at $L = 10$ m. The mid-plane is at the left side, and is a symmetry plane. The small inset on the right of each plot is a zoom-in of the last 20 cm in front of the target. The scales are kept the same in all sub plots, to allow an easy comparison of the differences. Plasma density n_p (green line) in units of 10^{19} m^{-3} and temperature T (orange dashed) in units of eV is plotted to the linear scale on the left hand side. The neutral density n_n (brown dash dotted) is plotted to the log scale on the right hand side. Plasma pressure p_n (10^{20} eVm^{-3}); left axis — blue dash double dotted — is the sum of static plasma pressure $n_p T$ and dynamic pressure nU^2 , plotted on the linear scale on the left. On the left hand side of the plot are simulations with an energy influx of 5 W/m^2 , right are profiles with an energy influx of 10 W/m^2 . The upstream densities n_0 are bottom to top $n_0 = 16 \cdot 10^{18}, 32 \cdot 10^{18}, 48 \cdot 10^{18}$ and $64 \cdot 10^{18} \text{ m}^{-3}$. The detachment front is highlighted by a shaded area.

value upstream. The energy influx is set to values in the range of 5 to 10 MW/m^2 and the 1D simulation were run to steady state. Fig. 1 shows some of the obtained backgrounds. With the exception of the bottom right figure, a significant temperature drop towards the target is observed. The plasma pressure, plotted with a blue dashed double dotted line stays mostly constant, until shortly before the target. The target pressure in fig 1 (a,c) drops to 20% of the upstream value, while in (g) the pressure stays basically constant along the flux tube, while in (b) the pressure drops to around $\frac{1}{3}$ of the upstream value. As the upstream plasma density increases, the region of increased neutral density extends along the field line, where the plasma temperature is low, and the plasma density is increased. As long as the pressure stays constant, a decrease in plasma temperature coincides with an increase in plasma density to conserve pressure. 0.5 m in front of the target the neutral density increases further, which causes the plasma pressure to decrease several cm in front of the target. The

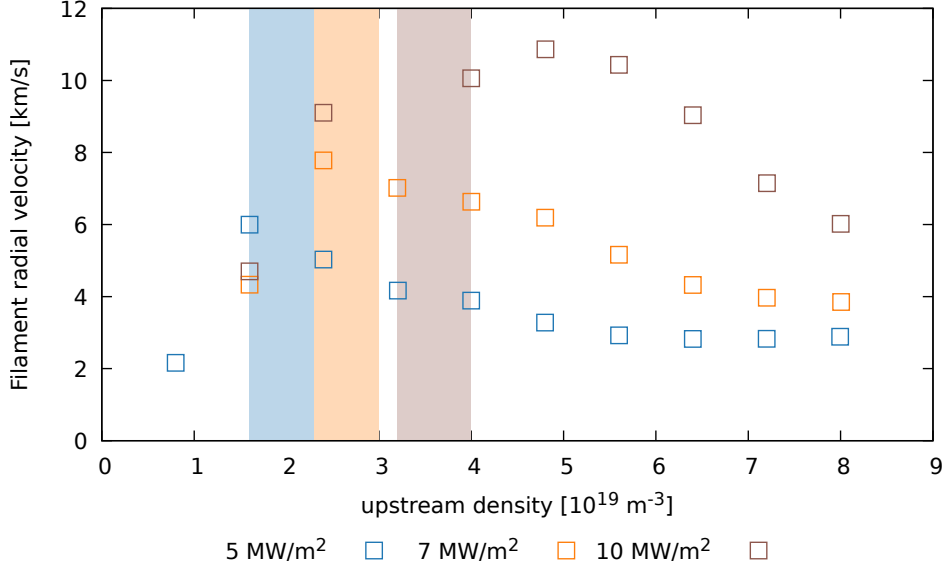


Figure 2: Particle target flux roll-over plot for different energy influxes, obtained with the described 1D model. Some of the profiles are shown in fig. 1. The shaded area represent detachment onset, according to the onset of pressure drop.

dependence of the particle target flux on the upstream density is shown in fig. 2. For the 7 and 10 MW/m² cases the particle target flux increases initially before it decreases for higher densities. In the 5 MW/m² case the roll-over happens below $2.4 \cdot 10^{18} \text{ m}^{-3}$. This means that most of the 5 MW/m² cases are detached, while only the higher density cases at 10 MW/m² are detached. Detachment on-set, featuring pressure drop, is indicated by the shaded areas for the respective energy influxes.

While this code produces detached solutions, the details may vary compared to more complex codes, such as SOLPS, due to the additional neutral physics, as for example no molecules are included, or the lack of the 2nd or 3rd dimension [10]. Further kinetic neutral effects, molecular effects, as well as effects due to a full geometry are neglected. As the three main interaction between plasma and neutrals are included, namely charge exchange, ionisation and recombination, It is expected that this model still captures the general trend and as it is the first study of interaction between filaments and detachment provides motivation for further, more complete studies. Thus the results are not expected to accurately predict experimental observation, but capture the lowest order effect of detachment on filament dynamics and thus give qualitative useful results concerning the phenomenology of filament motion in detached conditions.

4. Filament evolution

Filaments were seeded on the backgrounds discussed in sec. 3. They were seeded as a Gaussian perturbation in the drift plane, and with a tanh shape in the parallel direction, where the length was chosen as 5 m. In the perpendicular direction a Gaussian width of 2 cm was chosen for the initial studies [15], which was later varied to study the roll of δ_{\perp} .

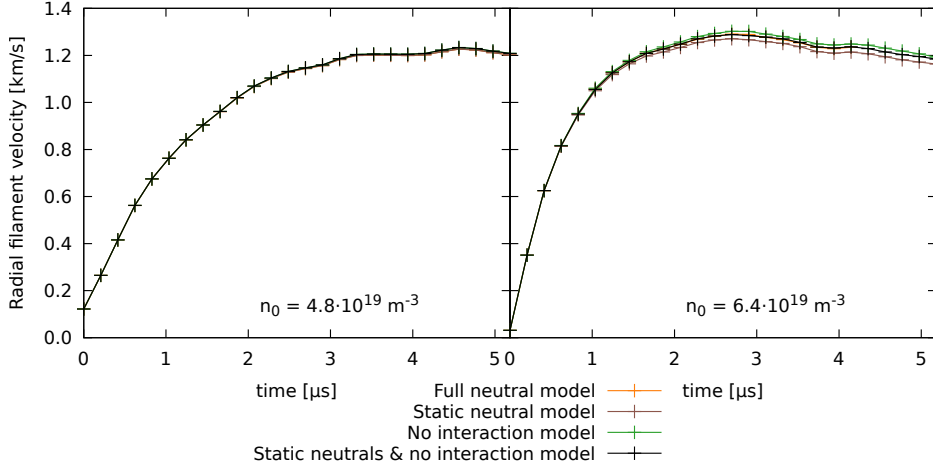


Figure 3: Time evolution of the radial velocity of a filament seeded on the background with 10 MW/m^2 and $n_0 = 48 \cdot 10^{18} \text{ m}^{-3}$ (left) as well as $n_0 = 64 \cdot 10^{18} \text{ m}^{-3}$ (right), shown in fig. 1(d,b). Results for different neutrals model are shown, see legend.

The perturbation for density and temperature was chosen equal to the upstream background value n_0 and T_0 . This keeps the relative perturbation $\frac{\delta n}{n_0}$ as well as $\frac{\delta T}{T_0}$ in all cases upstream constant, at $\frac{\delta n}{n_0} = \frac{\delta T}{T_0} = 1$.

The filament was evolved and the centre of density was tracked in the drift plane by taking the centre of mass above a threshold. This is described in more detail in our previous paper [15].

4.1. Direct influence of neutrals

Fig. 3 shows the time evolution of the radial velocity of a filament seeded on the high density backgrounds $n_0 = 48 \cdot 10^{18} \text{ m}^{-3}$ and $n_0 = 64 \cdot 10^{18} \text{ m}^{-3}$ in the 10 MW/m^2 case, shown in fig. 1(b,d). The no-interaction models in all cases show faster radial filament velocity than the version that includes the vorticity-neutral interaction, however the effect is below 1% in the $n_0 = 64 \cdot 10^{18} \text{ m}^{-3}$ case and not noticeable in the lower density cases.

In the $n_0 = 48 \cdot 10^{18} \text{ m}^{-3}$ case, keeping the neutrals static has basically no effect. In the $n_0 = 64 \cdot 10^{18} \text{ m}^{-3}$ case where the cold detachment front is within the seeded filament, the static neutral simulation over-estimates the influence of the neutrals by about 1.5%. This can be explained by looking at the plasma profiles, shown in fig. 4. In the $n_0 = 48 \cdot 10^{18} \text{ m}^{-3}$ case the cold plasma region does not extend into the seeded filament, and thus the neutral density is rather low in the seeded filament. In the $n_0 = 64 \cdot 10^{18} \text{ m}^{-3}$ case, the filament is seeded within the cold plasma region which includes a high neutral density. Thus in the $n_0 = 64 \cdot 10^{18} \text{ m}^{-3}$ case a significant amount of neutrals are ionized by the filament, unlike in the $n_0 = 48 \cdot 10^{18} \text{ m}^{-3}$ case.

4.2. Dependence on detachment

Compared to the previous study, in attached conditions, the velocity of filaments in these higher density simulations is decreased [15]. Previously the slowest filament

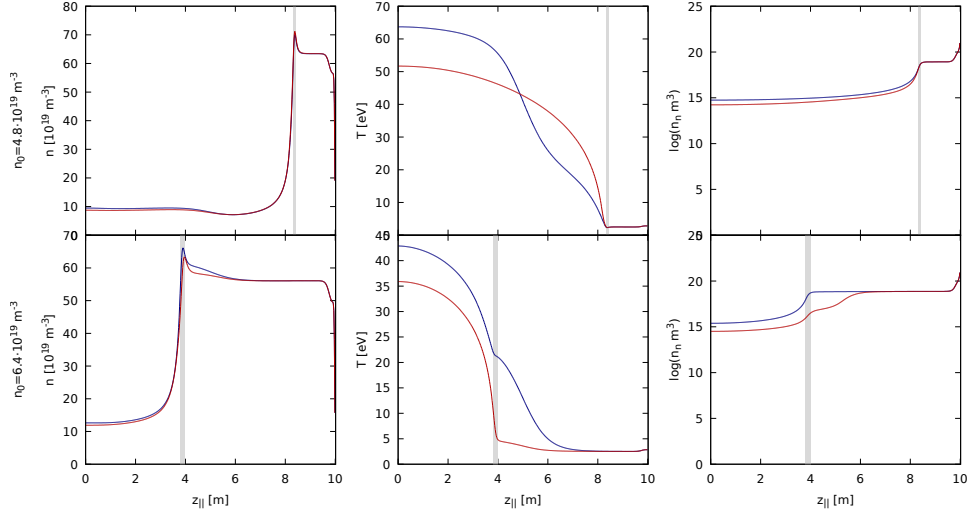


Figure 4: Plasma profiles at the centre of the filament. Shown in blue are the profiles just at the beginning of the simulation, before the neutrals could adjust to the perturbation. Shown in red are the profiles after $\approx 4 \mu\text{s}$. Shown is the plasma density (left), electron temperature (centre) and neutral density (right). On the top is the $n_0 = 48 \cdot 10^{18} \text{ m}^{-3}$ case, and on the bottom the $n_0 = 64 \cdot 10^{18} \text{ m}^{-3}$ case, both with 10 MW/m^2 energy influx, as shown in fig. 1(d,b). The detachment front is shaded in grey.

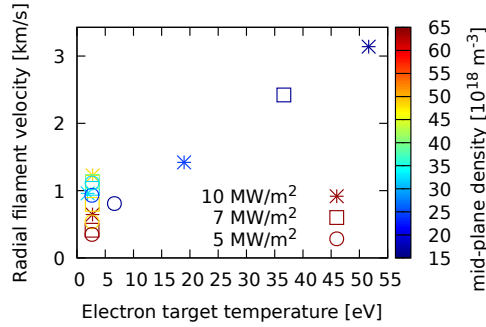


Figure 5: Peak radial filament velocity for the backgrounds shown in fig. 1 versus target temperature of the background. The target temperature dependency breaks down for target temperatures below 5 eV.

velocity reached was around 550 m/s at an target temperature of 0.8 eV. Higher target temperatures resulted in faster filament velocities. In the simulations presented here the target temperature does not drop below 2.5 eV, as the recombination acts as a heat source for the electrons at low temperatures. Fig. 5 shows the peak radial filament velocity versus the target temperature. While for the high target temperature cases the previous findings of a target temperature dependence are reproduced, this does not hold for target temperatures below ~ 5 eV. The main differences to the previous study is the increased plasma density, as well as the Franck-Condon energy source from ionisation.

To understand the dependence of the filament velocity in detached conditions,

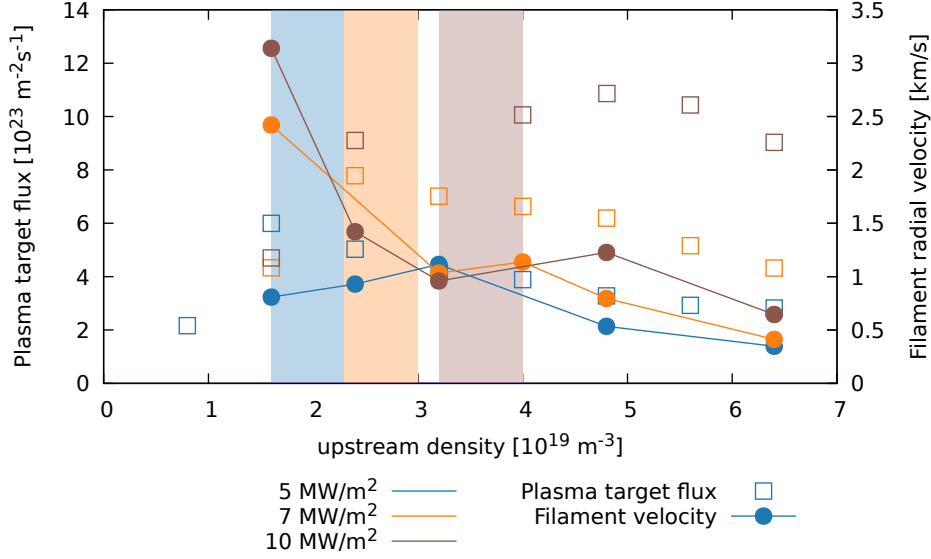


Figure 6: On the left axis is the particle target flux of the associated background profiles. On the right axis is the peak radial filament velocity for different plasma backgrounds. The lines are to guide the eye, and do not imply that the transition between the points would be linear. The shaded are represent detachment onset for the different energy influxes. A general decreasing trend of the radial velocity with increasing density is observed, except at the flux roll-over point, where the filaments become temporarily faster.

fig. 6 shows the filament velocity as a function of upstream density, as well as particle target flux of the associated backgrounds. The filament velocity generally decreases with increasing density. The 5 MW/m² case has an exception for densities less than $n_0 = 32 \cdot 10^{18} \text{ m}^{-3}$, the 7 MW/m² case between $n_0 = 32 \cdot 10^{18} \text{ m}^{-3}$ and $n_0 = 40 \cdot 10^{18} \text{ m}^{-3}$ and the 10 MW/m² case between $n_0 = 32 \cdot 10^{18} \text{ m}^{-3}$ and $n_0 = 48 \cdot 10^{18} \text{ m}^{-3}$. The particle target flux roll-over is at $n_0 = 16 \cdot 10^{18} \text{ m}^{-3}$, $n_0 = 24 \cdot 10^{18} \text{ m}^{-3}$ and $n_0 = 40 \cdot 10^{18} \text{ m}^{-3}$ respectively. In all three cases, with increasing density the target flux roll-over and pressure drop happen, and at even higher densities the radial velocity increases temporarily. This suggests that after detachment is reached, the filaments get faster, before the velocity begins to decrease again. At this point, a cold and dense plasma in front of the target is building up and with increased density as well as decreased temperature, the resistivity is significantly increased, which suppresses currents in the filament reaching the target. Fig. 7 shows the current density in the centre of the filament, for the 10 MW/m² cases. While in the attached cases, the currents flow to the target on the right hand side, in the detached cases the currents are only flowing to the edge of the cold plasma region, where strong currents due to the large density gradients are observed. The increase of the filament radial velocity with increased resistivity was predicted by Easy *et al* [12]. The decrease of the filament velocity with increasing density is at least partially due to a decreased drive as the temperature is decreased. In addition to an decreased drive, the plasma viscosity increases, which also reduces the filaments velocity. Thus in general the decreased drive and the increased viscosity are dominating over the increased parallel resistivity for most densities, with the exception after detachment is reached, where

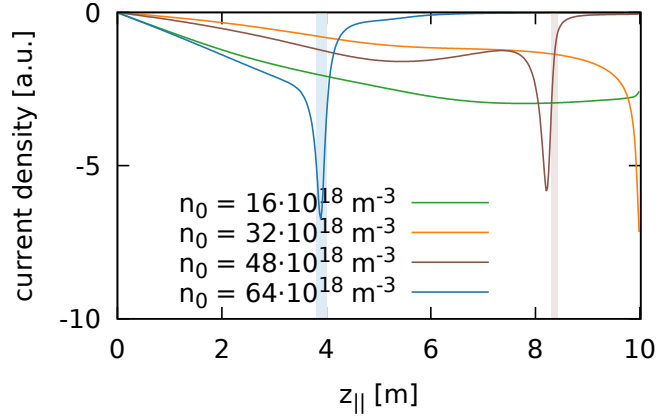


Figure 7: Current density at the centre of the filament after $\sim 4 \mu\text{s}$ for the 10 MW/m^2 cases shown in fig. 1(b,d,f,h). In the detached cases, currents near the target are strongly suppressed. The detachment front is shaded in the respective colour.

the velocities temporarily increase and the increased resistivity dominates over the other changes.

4.3. Dependence of critical size

The vorticity closing mechanism, and thus the dynamics of filaments strongly depends on the size of the filament with respect to the critical size δ^* . For small filaments, i.e. $\delta_{\perp} < \delta^*$, the vorticity is closed mostly in the drift plane, and the filament velocity increases monotonically with size. For large filaments, the vorticity is closed predominantly via parallel dynamics, and a monotonic decrease with filament size is expected.

To further understand the influence of detachment on filament dynamics, different sized filaments were seeded on the background profiles. The result of the filament size scan is shown in fig. 8. Also shown is the critical size, as determined by fitting a quadratic function in log-space using gnuplot [24]. Additionally to the full model, a second case is run where the perpendicular viscosity is set to zero. While the perpendicular diffusion constants are physically motivated, the real value is not known. Some models don't include viscosity or diffusion at all [6,25]. The previous study found a strong viscosity dependence of the filament dynamics, thus the viscosity dependence was once more investigated. The neo-classical viscosity values were assumed to be the upper bound and setting the viscosity to zero is a natural lower bound. Thus the resulting error of this uncertainty is expected to be bound by the full model on one side, and by the no-viscosity case on the other hand.

In the filament size scan in attached conditions, the regime transitions from the viscous regime for small filaments to the sheath limited regime for large filaments, where sheath currents are the main current closing mechanism. In detached conditions, for small filaments, the vorticity is mainly closed by viscosity. For large filaments, sheath current can no further close the vorticity, as sheath currents are strongly suppressed, as shown in fig. 7. As mentioned earlier, the filament scaling expected

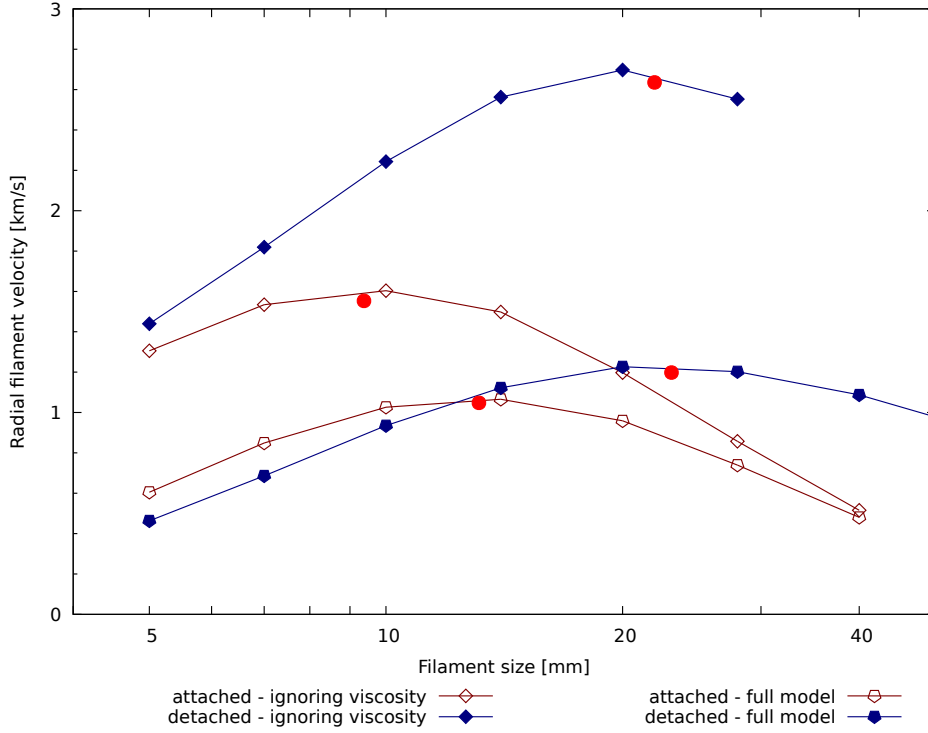


Figure 8: Peak radial filament velocity for different sized filaments. The blue, filled symbols are in detached conditions (10 MW/m^2 , $n_0 = 32 \cdot 10^{18} \text{ m}^{-3}$, fig. 1(f)), while the red, open symbols are in attached conditions (10 MW/m^2 , $n_0 = 48 \cdot 10^{18} \text{ m}^{-3}$, fig. 1(d)). The downward pointing triangles are from simulations using the full model, whereas the upward pointing triangles are from simulations ignoring the perpendicular viscosity. The fitted position of the critical size is shown as red dots.

for neutrals does not have a size dependence. As with increasing size the monotonic decrease is retained, while the high resistivity strongly reduces sheath currents, sheath currents are not fully suppressed. Looking at the contributions in the vorticity equation, it can be observed that the viscosity contribution is increasing for filaments until $\delta_{\perp} \approx 20 \text{ mm}$. While the viscosity contribution within the filament decreases with increasing size, the contribution at the detachment front shows a more complicated behaviour. While for small filaments the vorticity is closed locally, for large ones the vorticity is advected towards the sheath, and as the viscosity is more effective at higher density and lower temperature, the viscosity still provides a significant closing mechanism at the front of the detached volume, but decreases quickly with increasing size due to the δ_{\perp}^{-2} dependence.

As the viscosity closure is decreasing with increasing size, the impact of the neutrals is increasing. For the $\delta_{\perp} = 20 \text{ mm}$ filament, the neutrals contribution is roughly $\frac{1}{60}$ of the viscosity contribution, while in the $\delta_{\perp} = 40 \text{ mm}$ case the neutrals have nearly doubled their impact, and the neutrals contribution is about $\frac{1}{20}$ of the viscosity contribution.

In the full model, the filaments of 14 mm and larger are faster in the detached condition than in attached conditions. This is expected, as small filaments are not influenced by sheath currents, and the increased viscosity, resulting from the higher density in detached state will thus reduce the velocity the filament achieves. For large filaments, the suppression of sheath currents is much more important and the effect of viscosity is weaker, thus they are faster in detached conditions. In the case without viscosity, the filaments of all sizes, down to 5 mm are faster in the detached condition than in the attached case. This indicates that even for 5 mm filaments, in the absence of perpendicular viscosity, parallel dynamics plays a role, as a significant part of the vorticity is advected towards the target. In the low resistivity, attached case, sheath currents provide a monopole contribution, and the $E \times B$ term causes a significant contribution to the vorticity sink. In the high resistivity case, the $E \times B$ contribution is significantly reduced. In that case parallel advection and diffusion are preventing further acceleration of the filament. Therefore in the absence of viscosity, even the small filaments are influenced by the sheath conditions, thus filaments of all sizes achieve higher velocities in detached conditions, where sheath effects are suppressed.

The full model as well as the no viscosity model, show a higher increase in velocity with detachment for larger filaments. Further, the critical size δ^* increases significantly with detachment. Note that δ^* is defined as the perpendicular size where filaments are fastest.

To put these results further into context, the scan has been extended to more densities, as shown in fig. 9 The density dependence of filaments of $\delta_{\perp} = 20$ mm has already been discussed in section 4.2. The trend is the same for larger filaments as well, though small filaments (10 mm and smaller) show a monotonic decrease with increasing density. In attached conditions the critical size δ^* decreases with increasing density. This is in contrast to our previous study, where a increase with increasing density was observed. The main difference between the two studies is, that here the energy influx was kept constant, whereas in the previous study, the upstream temperature was kept constant [15]. In the case of a fixed heat flux, an increased density results in an decreased temperature, due to pressure conservation. It seems thus that the decreasing temperature reduces the critical sizes stronger, then the density increases the critical size. As detachment is reached, the critical size δ^* shifts dramatically to larger sizes. This can be explained by the suppression of sheath currents, which allows larger filaments to reach higher velocities. As larger filaments are faster, the critical size is shifted towards larger sizes. Fig. 9 contains also a plot of the critical sizes plotted against the respective densities. The critical size was determined by fitting a quadratic function against the radial velocity versus logarithm of the perpendicular size using gnuplot [24]. In the $n_0 = 64 \cdot 10^{18} \text{ m}^{-3}$ case the critical size is further increased with respect to the $n_0 = 48 \cdot 10^{18} \text{ m}^{-3}$ case, which is already detached. This demonstrates the importance of how far the detachment has moved toward the X-point, which roughly linearly increases the collisionality integrated along the flux tube.

For experimentally observed filaments, it is expected that filaments in detached conditions are generally slower than in fully attached conditions, however not a simple relationship with detachment is expected, but rather filament size δ_{\perp} with respect to the critical size δ^* needs to be taken into account.

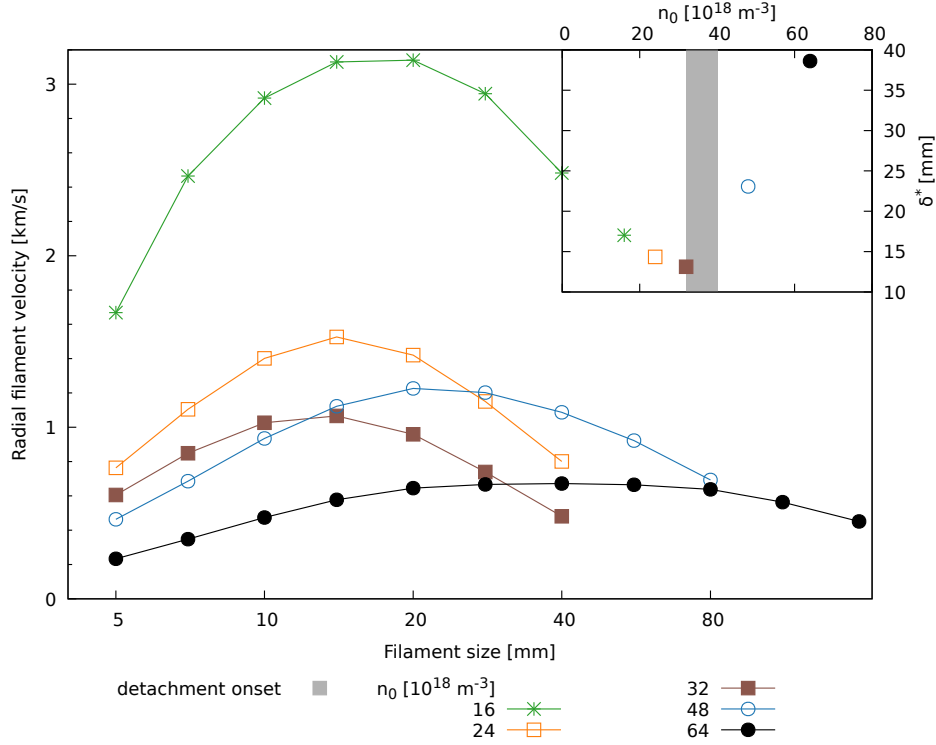


Figure 9: Peak radial filament velocity for different sized filaments for different backgrounds. The backgrounds have an energy influx of 10 MW/m^2 , and the densities range from $n_0 = 16 \cdot 10^{18} \text{ m}^{-3}$ to $n_0 = 64 \cdot 10^{18} \text{ m}^{-3}$. On the top right is the critical size of for the different densities. The shaded region denotes the onset of detachment.

4.4. Rigidity of filaments

Filaments have been observed to bend in electro-magnetic models, where the pressure perturbation is not more much smaller than the magnetic pressure [25]. The model used here however uses the electrostatic assumption, and in previous studies the filaments have been observed to be rigid. The radial displacement of the filaments seeded on the backgrounds shown in fig. 1 has been computed for the different x - y -slices along z_{\parallel} and is shown in fig. 10. In attached conditions, the velocity has no z_{\parallel} dependence, and the filament moves rigidly. Also in detached conditions, the filaments in $n_0 = 48 \cdot 10^{18} \text{ m}^{-3}$ 10 MW/m^2 as well as $n_0 = 32 \cdot 10^{18} \text{ m}^{-3}$ 5 MW/m^2 still move rigidly. Only the filaments in $n_0 = 64 \cdot 10^{18} \text{ m}^{-3}$ with 10 MW/m^2 and 5 MW/m^2 as well as $n_0 = 48 \cdot 10^{18} \text{ m}^{-3}$ 5 MW/m^2 show bending. In addition all showing a low radial velocity, the filaments that bend have in common that they were seeded partially within the detached region. This prevents currents within the filament to flow freely, which explains why the advection within the filament is strongly dependent on the position within the filament. In fig. 10(a,c) the first 3 meters of the filament move mostly rigidly, and for (b) the first 2 m - which coincides with the non-detached region in fig 1. Whilst this is clearly an idealised scenario, the deviation of filaments from field

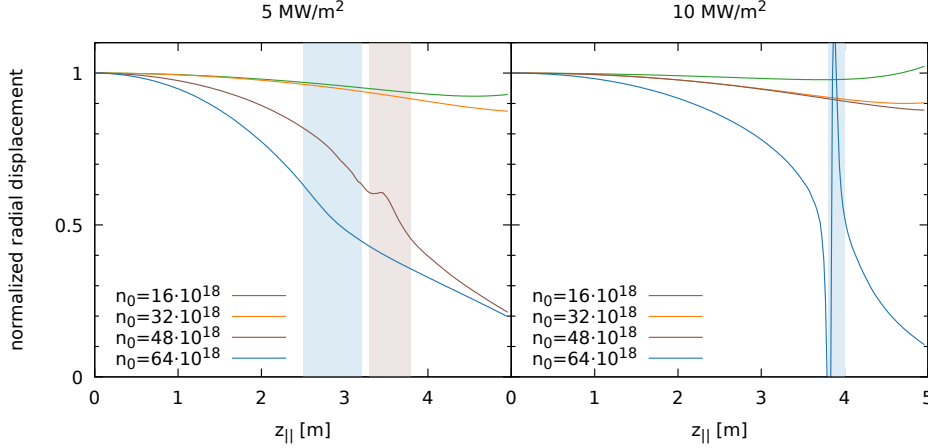


Figure 10: Dependence of the filaments radial displacement on the parallel direction $z_{||}$ for the different backgrounds in fig. 1. The displacement was normalized to the displacement at $z_{||} = 0$. Note that only the upper half of the domain is plotted, where the filament was. The detachment front is represented by a shaded area. In the $n_0 = 64 \cdot 10^{18} \text{ m}^{-3}$ 10 MW/m² case the detection did not work reliably around $z_{||} \approx 4$ m, as the background density features strong parallel gradients, thus small movements of the detachment front making the detection of the centre of the filament unreliable.

alignment in detached plasmas may be a useful result for experimental comparison.

5. Discussion

Similar to the previous study, strictly in attached conditions, keeping the neutrals fixed at their background values has only a minor impact on the dynamics of filaments. If filaments are able to penetrate into a detached region, they can ionise significant amount of neutrals, which may be relevant to detachment burn-through studies, however. Burn-through is not studied in this paper, as the neutral code was unstable close to re-attachment.

Easy *et al* predicted that a cold divertor could increase the radial velocity of filaments, as well as the critical size δ^* due to a rise in collisional resistivity [12]. While both an increase in radial velocity as well as an increase of δ^* has been observed as detachment is reached, the increase of the radial velocity is rather weak, and a hotter divertor yields higher radial velocities in general. It has been suggested that detachment, or more generally a high collisionality in the divertor could be the cause of SOL flattening, as the high resistivity could be preventing sheath currents, and thus increase the radial filament transport [26]. This study shows that collisionality may be responsible for a change of filament dynamics, rather than e.g. the increased neutral density. However, the increase of filament velocities with detachment is well below the radial velocities in sheath limited conditions, so this study does not support the hypothesis that shoulder formation is the result of high divertor collisionality and increased filament transport fluxes.

Furthermore, as a high plasma density as well as a low plasma temperature is required to achieve a sufficiently high resistivity to sufficiently prevent sheath currents

to influence the filament dynamics, this will most likely be not the case in the far SOL, thus even if the acceleration caused by detachment is higher than suggested by these simulations, the velocity should quickly drop, once the filament is connected to a lower density region and thus can connect to the target.

After detachment occurs, a strong increase of the critical size of filaments with increasing density is observed. In attached conditions a weak reduction of the critical size with increased density is observed, which is associated with a reduction of the temperature as the energy influx is kept constant. After detachment occurs, cold and dense plasma at the target is suppressing sheath currents, and with increasing density the detachment volume is increasing, thus shifting the critical size higher. While neutrals can partially compensate for the lack of sheath currents, the vorticity sink due to neutrals is over an order of magnitude smaller than the sink due to viscosity.

The observed filament bending agrees with Easy *et al* where bending was observed if the resistivity was uniformly enhanced, whereas a localized resistivity at the target resulted in a rigid filament [12]. Note that this bending mechanism wouldn't be expected to be observed in experiments. The bending was only observed in cases where the detachment front has moved quite far upstream.

Easy *et al* increased the resistivity artificially by a factor of 10 000 and estimated that the temperature at the divertor would need to drop to 0.086 eV compared to the 40 eV reference case [12]. The estimates assumes that the resistivity has a temperature dependency $\nu_{\parallel} \propto T^{-3/2}$. However, the resistivity also has a density dependence i.e. $\nu_{\parallel} \propto n \cdot T^{-3/2}$. If we assume that the pressure $n \cdot T$ is preserved (same upstream conditions but colder divertor) the scaling can be expressed again in terms of the temperature: $\nu_{\parallel} \propto T^{-5/2}$. Thus achieving the 10 000 increase only requires 1 eV - which is much closer to the temperatures reached here and may explain why the bending effect is seen in the detached simulations.

While Easy *et al* predicted that the velocity will be increased with increased resistivity, the self-consistent simulations conducted here show that the increase with detachment is significantly smaller, than the net decrease with respect to attached simulations, where target temperatures above 25 eV reach velocities exceeding 2 km/s - whereas in detached conditions only about 1 km/s was reached. However, a change in the transition of filament dynamics from inertial or viscous to sheath-limited is observed and the critical size of filaments δ^* increases dramatically after detachment.

6. Summary

The paper presents attached as well as detached 1D parallel plasma profiles and the dynamics of filaments in a 3D slab geometry seeded on these profiles. The detachment features particle target flux roll-over as well as a significant plasma pressure drop. Detachment was achieved by using a refined neutral model, which is able to capture and evolve steep gradients in the neutral density, which is observed in near the target.

In terms of dependence of the filament dynamics on the background conditions, a general decreasing trend of radial filament velocity with increasing plasma density is observed. This trend is temporarily broken as detachment is entered, where especially large filaments are faster than before detachment. This is caused by the higher parallel resistivity. This also causes an increase of the critical size, which further increases as the detachment front moves further upstream and the integrated resistivity increases.

While detachment can increase the radial velocity, the observed radial filament velocities in hotter, attached plasmas are still higher than the ones observed in

detachment.

7. Acknowledgement

This work has been carried out within the framework of the EUROfusion Consortium and has received funding from the Euratom research and training programme 2014-2018 and 2019-2020 under grant agreement No 633053. The views and opinions expressed herein do not necessarily reflect those of the European Commission. This work used the EUROfusion High Performance Computer (Marconi-Fusion) through EUROfusion.

- [1] D'IPPOLITO, D. et al., *Physics of Plasmas* (1994-present) **18** (2011) 060501.
- [2] WALKDEN, N. et al., *Nuclear Materials and Energy* **12** (2017) 175 , Proceedings of the 22nd International Conference on Plasma Surface Interactions 2016, 22nd PSI.
- [3] BOEDO, J. A. et al., *Physics of Plasmas* **8** (2001) 4826.
- [4] WALKDEN, N. et al., <https://github.com/boutproject/BOUT-dev/blob/master/examples/boutcore/blob2d.py>, Accessed 6 Mar 2019.
- [5] EASY, L. et al., *Physics of Plasmas* **21** (2014).
- [6] ANGUS, J. R. et al., *Phys. Rev. Lett.* **108** (2012) 215002.
- [7] JOVANOVIĆ, D. et al., *Physics of Plasmas* (1994-present) **15** (2008) 112305.
- [8] POTZEL, S. et al., *Nuclear Fusion* **54** (2014) 013001.
- [9] HUTCHINSON, I., *Nuclear Fusion* **34** (1994) 1337.
- [10] WISCHMEIER, M. et al., *Journal of Nuclear Materials* **390–391** (2009) 250 , Proceedings of the 18th International Conference on Plasma-Surface Interactions in Controlled Fusion Device Proceedings of the 18th International Conference on Plasma-Surface Interactions in Controlled Fusion Device.
- [11] COSTER, D., *Journal of Nuclear Materials* **415** (2011) S545 , Proceedings of the 19th International Conference on Plasma-Surface Interactions in Controlled Fusion.
- [12] EASY, L. et al., *Physics of Plasmas* (1994-present) **23** (2016) 012512.
- [13] MILITELLO, F. et al., *Nuclear Fusion* **56** (2016) 104004.
- [14] MILITELLO, F. et al., *Physics of Plasmas* **25** (2018) 056112.
- [15] SCHWÖRER, D. et al., *Plasma Physics and Controlled Fusion* **61** (2018) 025008.
- [16] WALKDEN, N. R. et al., *Plasma Physics and Controlled Fusion* **58** (2016) 115010.
- [17] SCHWÖRER, D. et al., *Nuclear Materials and Energy* **12** (2017) 825 .
- [18] DUDSON, B. D. et al., *Plasma Physics and Controlled Fusion* **50** (2008) 124012.
- [19] DUDSON, B. D. et al., *Journal of Plasma Physics* **81** (2015).
- [20] WISING, F. et al., *Contributions to Plasma Physics* **36** 309.
- [21] DUDSON, B. D., <https://github.com/boutproject/SD1D/tree/master/doc>, 2017, Version 1538638; Accessed Sept 2018.
- [22] WESSON, J. et al., (2004).
- [23] FUNDAMENSKI, W. et al., *Nuclear Fusion* **47** (2007) 417.
- [24] WILLIAMS, T. et al., *Gnuplot 5.0: an interactive plotting program*, <http://gnuplot.sourceforge.net/>, 2016.
- [25] LEE, W. et al., *Journal of Nuclear Materials* **463** (2015) 765 , PLASMA-SURFACE INTERACTIONS 21.
- [26] CARRALERO, D. et al., *Nuclear Materials and Energy* **12** (2017) 1189 , Proceedings of the 22nd International Conference on Plasma Surface Interactions 2016, 22nd PSI.
- [27] TANGE, O., *GNU Parallel 2018*, Ole Tange, 2018.